Segmentation of Retinal Arteries in Adaptive Optics Images

Nicolas Lermé*, Florence Rossant*, Isabelle Bloch†, Michel Paques‡ and Edouard Koch‡
* Institut Supérieur d'Électronique de Paris
† Institut Mines-Télécom, Télécom ParisTech, CNRS LTCI
‡ CIC 503, Centre Hospitalier National des Quinze-Vingts

***Abstract*—In this paper, we present a method for automatically segmenting the walls of retinal arteries in adaptive optics images. To our best knowledge, this is the first method adressing this problem in such images. To achieve this goal, we propose to model these walls as four curves approximately parallel to a common reference line located near to the center of vessels. Once this line detected, the curves are simultaneously positioned as near as possible to the borders of walls using an original tracking procedure to cope with deformations along vessels. Then, their positioning is refined using a deformable model embedding a parallelism constraint. Such an approach enables us to control the distance of the curves to their reference line and improve the robustness to image noise. This model was validated on healthy subjects by comparing the results against segmentations from physicians. Noticeably, the variability introduced by this model is smaller or very near to the inter-physicians variability.**

Keywords: Active contours model, adaptive optics, approximate parallelism, retina imaging.

I. Introduction

Arterial hypertension (AH) and diabetic retinopathy (DR) mainly and precociously affect the physiology and structure of retinal blood vessels of small diameter (i.e. less than 150μm). According to the Public Health Agency of Canada, AH and DR affected 15 to 20% of the world's adult population in 2009. These modifications can result in a thickening or a narrowing of walls and are predictive of end-organ damage such as stroke or visual loss [4], [3]. For instance, the authors of [13] estimate that 98% of visual damages could be avoided if DR was treated in time [13]. Accurate measurements of walls are therefore of crucial importance to better prevent the DR and the complications of AH. However, classical fundus photographs and Doppler-based measurements cannot capture such level of details due to their limited spatial resolution.

Adaptive-Optics (AO) based cameras improve the lateral resolution of fundus photographs, thus enabling the visualization of microstructures such as photoreceptors [10], capillaries [11] and vascular walls [1], noninvasively. In the present study, the camera rtx1 [14] is used to acquire 2D images by flood illumination at 10Hz using a 850nm LED light source with a pixel-resolution of 0.8μm. Flood-illumination systems usually produce noisy images making walls hardly visible. A commonly used solution is to register these images and average them to increase the signal-to-noise ratio [9]. In the latter, blood vessels appear as dark elongated structures with a bright linear axial reflection, over a textured background. Outer borders of walls are however only visible along arteries and the present study will therefore focus on them. Parietal structures (arterial walls) appear as a gray line along both sides of the lumen (blood column), with a typical thickness of about 15% of the latter [7] (see Figure 1).

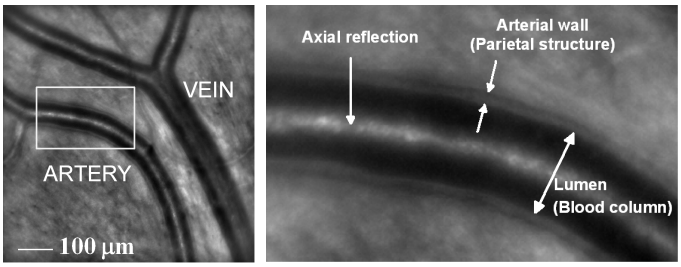

Figure 1: A mean image obtained with [9] (left) and a detailed view of an artery (right).

In this paper, we propose an automatic procedure for segmenting arterial walls in a selected region of interest [1] in the mean images produced by [9]. To our best knowledge, this is the first method adressing this problem in such images. This task is challenging for multiple reasons: (i) background is highly textured, (ii) lumens are globally dark but with significant intensity variation along them, (iii) axial reflections may locally show discontinuities or poor contrast, (iv) outer borders of walls are low-contrasted, (v) segments can be locally blurred due to the geometry of the retina, and (vi) deformations can occur along vessels in case of pathologies.

To overcome these difficulties, we propose a strategy exploiting geometric, radiometric and topological *a priori* information of vessels. More precisely, we model arterial walls as four curves approximately parallel to a common reference line located near to the axial reflection. Once this line detected, the curves are simultaneously positioned as near as possible to the borders of walls using a tracking procedure to cope with deformations along vessels. Then, their positioning is refined using [5] where curves evolve towards large image gradients under a parallelism constraint. Such an approach enables us to control the distance of the curves to their reference line and improve the robustness to image noise. We also mention that this work has permitted to establish relationships between morphometric measurements and clinical parameters [8].

This work is funded by the Institut National de la Santé et de la Recherche Médicale and the Agence Nationale pour la Recherche (ANR-09-TECS-009 and ANR-12-TECS-0015-03) for the period 2013–2015.

[1] In particular, we do not aim at segmenting the whole vascular tree. This problem will be the subject of a forthcoming paper.

The remaining of this paper is organized as follows. In Section II, we first summarize the steps for detecting axial reflections. Then, we detail in Section III the procedure for segmenting the arterial walls. Finally, we evaluate the relevance of the approach in Section IV and conclude in Section V.

II. Axial reflection detection

In this section, we consider images as functions mapping points from $\Omega \subset Z^2$ into the interval $[0, 1]$.

A. Pre-processing

The original image (see Figure 2(a)) is first enhanced by applying a median filter followed by a non-linear diffusion filter [15]. This combination of filters allows us to denoise the image and smooth the blood vessels while preserving the contrast along their edges. We denote by I_P the resulting image (see Figure 2(b)).

B. Detection of bright elongated structures

To enhance the bright elongated structures, a white top-hat transform is applied on the pre-processed image I_P with a binary disk whose radius is 6 pixels (denoted by I_T, see Figure 2(c)). We binarize the resulting image I_T by hysteresis thresholding and denote it by I_{ES} (see Figure 2(d)). Parts of the axial reflection of vessels are thus extracted, but also other bright areas of the textured background. Further processing steps are therefore necessary to discard these undesired areas.

C. Detection of the darkest areas

K-means classification ($k = 3$) is performed on the pre-processed image I_P (see Figure 2(e)) and the cluster of lowest center provides a first binary image of the darkest regions. It is then post-processed with morphological operations to get the main connected components of the dark areas of lumens. The resulting image is denoted by I_{DA} (see Figure 2(f)).

D. Extraction of vascular segments by information fusion

A first selection of vascular segments is performed based on a simple measure of the tortuosity. Let us denote by I^L_{ES} the binary image of a tested connected component of the image I_{ES}. This component is retained if

$$\frac{\sharp I^L_{ES}}{\sharp (I^L_{ES} \bullet S)} > 0.8, \tag{1}$$

where $\sharp$ denotes the cardinality of a set, $\bullet$ denotes the closing operator and S is a binary disk whose radius is 15 pixels. Moreover, a segment of axial reflection must lie inside a dark area, and conversely, a dark region of the lumen must contain at least one axial reflection segment. We denote by $I_{ES'}$ the binary image made of the components satisfying (1) and $I^L_{ES'}$ a tested connected component of it. Such a component is kept as part of an axial reflection segment if

$$\sharp (I_{DA} \cap (I^L_{ES'} \oplus S')) > \frac{\sharp I^L_{ES'}}{5}, \tag{2}$$

where $\oplus$ denotes the dilation operator and S' is a binary disk whose radius is 15 pixels (in accordance to the minimum size of the vessels that are studied). We denote by $I_{ES''}$ the binary image made of the components satisfying (2) (see Figure 2(g)). Morphological operations are applied to I_{DA}, including reconstruction by dilation with the marker $I_{ES''}$, in order to get the final lumen mask I_{LM} (see Figure 2(h)).

E. Segment labeling and reconnection

We first compute the skeleton of the image $I_{ES''}$ to get the end-points of the retained segments (see Section II-D). These end-points are then reconnected using minimal path techniques [2], [12]. Theses techniques aim at extracting curves of minimal length, in a Riemannian metric computed from the image and depending on the targeted application. A minimal path C connecting two end-points p and q is obtained by minimizing the following functional:

$$L[C] = \int_p^q \mathcal{P}(C(s))\ ds,$$

where s denotes the curvilinear abscissa and $\mathcal{P}$ is a potential inducing the metric defined as

$$\mathcal{P}(x) = w_1(1 - I_T(x))^2 + w_2(1 - I_{SM}(x))^2 + w_3, \quad \forall x \in \Omega,$$

where I_{SM} is the spurred skeleton of the lumen mask I_{LM} filtered by a Gaussian of standard deviation σ and $w_1, w_2, w_3 \in \mathbb{R}^+$ are free parameters. These parameters are empirically set with $\sigma = 10$, $w_1 = 0.5$, $w_2 = 0.45$ and $w_3 = 0.05$. In the latter expression, the first term is derived from the top-hat image I_T (considering that the values should ideally be close to one along the axial reflection) while the second one encourages the path C to pass near the middle of the lumen mask I_{LM}. The last term is a regularization constant. The combination of the above criteria allows to have a good robustness against the variety of the encountered images.

Two end-points form a candidate pair for reconnection if they belong to the same connected component in the lumen mask I_{LM} and if they do not belong to the same connected component in the image $I_{ES''}$. The candidate pairs are then processed by decreasing order of the Euclidian distance (to start with points that are close to each other) and reconnected using the above procedure. A new skeleton is then calculated, providing the axial reflection of the vessels, and the vessel branches are then labeled (see Figure 2(i)). The vessel branchs are individually regularized using a classical parametric active contour [6] with Gradient Vector Flow [16]. The lumen mask I_{LM} is also labeled such that every non-null pixel receives the label of the closest branch (see Figure 2(j)).

III. Segmentation of arterial walls

For convenience, we detail the procedure for segmenting arterial walls on a single regularized vessel branch obtained at the end of the axial reflection detection step (see Section II). We denote this regularized branch as the reference line $V(s) = (x(s), y(s))^T$ of the vessel, parameterized by s. Once obtained, this line is considered to be fixed and will therefore no longer evolve in the subsequent steps. Additionally, we choose to model the walls as four curves approximately parallel to this line. We respectively denote by V_1, V_2 and V_3, V_4 the inner

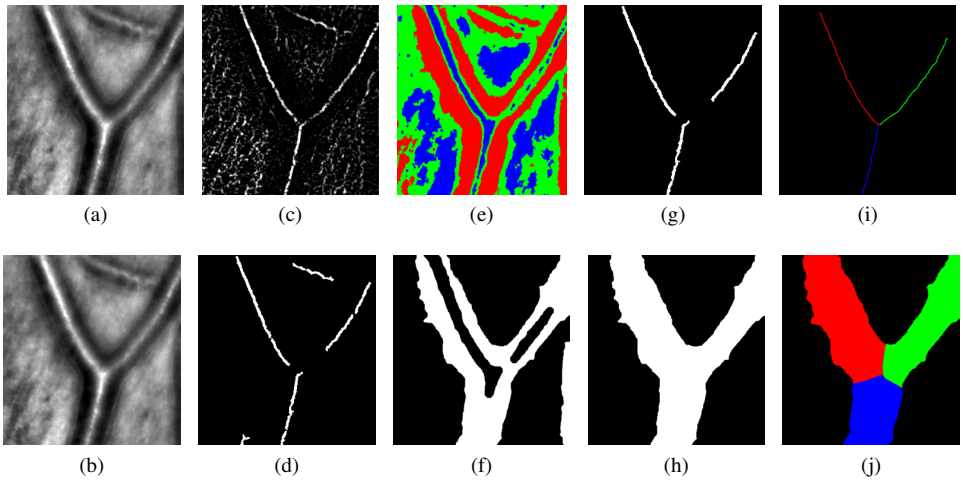

Figure 2: Steps for axial reflection detection: The source image (a) is first pre-processed (b). Dark elongated structures are detected from (b) by top-hat filtering (c) followed by hysteresis thresholding (d). Darkest areas are detected from (b) by k-means classification (e) followed by post-processing (f). Axial segments (g) and dark regions of lumens (h) are extracted from (d) and (f). Axial segments (i) and dark regions of lumens (j) are finally labeled from (c), (g) and the spurred skeleton of (h).

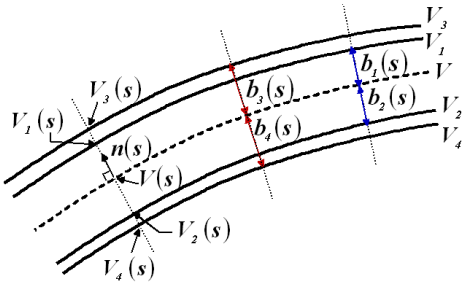

Figure 3: Parametric representation of the proposed model.

and outer borders of walls, and define them by

$$\begin{cases} V_1(s) &= V(s) &+ &b_1(s)\vec{n}(s) \\ V_2(s) &= V(s) &- &b_2(s)\vec{n}(s) \\ V_3(s) &= V(s) &+ &b_3(s)\vec{n}(s) \\ V_4(s) &= V(s) &- &b_4(s)\vec{n}(s), \end{cases}$$

where $\vec{n}(s)$ is the normal vector to the curve V and $b_k(s)$ is the local distance between the reference line V and the curve V_k, $\forall k \in \{1, \ldots, 4\}$ (see Figure 3). This model allows a direct correspondence between each curve V_k and the reference line V. In what follows, we describe a tracking procedure for roughly positioning these curves near to the borders of walls. Next, we detail the model used to refine their positioning.

A. Pre-segmentation

First, we discretize the reference line V in m equally spaced points and denote by $V_i = (x(s = ih), y(s = ih))^T$ the discrete coordinates at the point V_i and $\vec{n}_i$ the associated normal vector (h is the discretization step). We also discretize the curves representing the walls with

$$\begin{cases} V_i^1(b_i^{int}) &= V_i + b_i^{int}\vec{n}_i \\ V_i^2(b_i^{int}) &= V_i - b_i^{int}\vec{n}_i \\ V_i^3(b_i^{ext}) &= V_i + b_i^{ext}\vec{n}_i \\ V_i^4(b_i^{ext}) &= V_i - b_i^{ext}\vec{n}_i, \end{cases} \tag{3}$$

where b^{int} and b^{ext} respectively denote the half-diameter of the inner and outer borders. Such definition assumes that the inner and outer borders lie at the same distance from the reference line V. Although this assumption could appear to be strong, it is verified for a large number of the images presented in Section I. Also, the presegmentation described below leads to a preliminary result which will be refined in Section III-B.

Let us now denote by I a grayscale image with values in $[0, 1]$. We denote by $D_{\vec{u}}I(p)$ the derivative of I in the direction $\vec{u}$ at the point p. Moreover, for an half-diameter $b \in \mathbb{R}^+$, a point V_i and a window of size $(2r + 1)$, we define the mean intensity along the curves V^1 and V^2 by

$$\bar{I}^{int}(b, i, r) = \frac{1}{2(2r+1)} \sum_{j=-r}^{+r} \Big(I(V_{i+j}^1(b)) + I(V_{i+j}^2(b)) \Big), \tag{4}$$

the mean local gradient along the curves V^1 and V^2 by

$$\bar{D}^{int}(b, i, r) = \frac{1}{2(2r+1)} \sum_{j=-r}^{+r} \Big(D_{\vec{n}_{i+j}} I(V_{i+j}^1(b)) + D_{-\vec{n}_{i+j}} I(V_{i+j}^2(b)) \Big), \tag{5}$$

and the mean local gradient along the curves V^3 and V^4 by

$$\bar{D}^{ext}(b, i, r) = \frac{1}{2(2r+1)} \sum_{j=-r}^{+r} \Big(|D_{\vec{n}_{i+j}} I(V_{i+j}^3(b))| + |D_{-\vec{n}_{i+j}} I(V_{i+j}^4(b))| \Big). \tag{6}$$

Increasing the window radius r makes gradient measures more robust to noise but less reliable where strong deformations occur along vessels. This parameter therefore requires a trade-off. Not using absolute values on directional derivatives in (5) allows to distinguish negative derivatives (near to the axial reflection) from positive ones (near to the inner borders of walls). We detail below the steps necessary to estimate the half-diameters b^{int} and b^{ext} in (3).

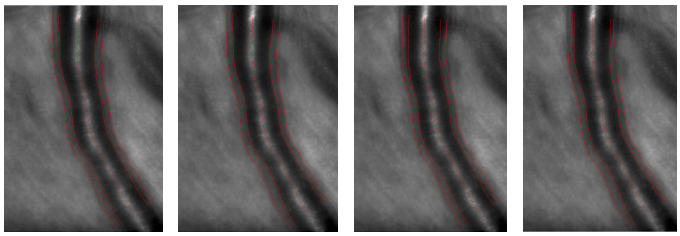

(a) (b) (c) (d)

Figure 4: Benefit of using a presegmentation with varying half-diameters (a),(b) against constant ones (c),(d) for a pathological case. Here, we set $r = 10$ and $\alpha = 0.95$. In (a) and (c), the image is superimposed with the presegmentations while it is superimposed in (b) and (d) with the segmentations obtained using the model described in Section III-B.

Step 1

We jointly search for a constant half-diameter of inner and outer borders maximizing the mean gradient divided by the mean intensity along the curves V^1 and V^2 plus the mean gradient along the curves V^3 and V^4. Using Equations (4), (5) and (6), such half-diameters are given by

$$(b'^{int^*}, b'^{ext^*}) = \underset{\substack{b'^{int}, b'^{ext} \\ b'^{int} < b'^{ext}}}{\operatorname{argmax}} \Big[\frac{\sum_i \bar{D}^{int}(b'^{int}, i, r)}{\sum_i \bar{I}^{int}(b'^{int}, i, r)} + \frac{1}{m} \sum_i \bar{D}^{ext}(b'^{ext}, i, r) \Big], \quad (7)$$

where we remind that m is the number of discrete points on V. Dividing by the intensity encourages gradients in dark areas. To speed up this step, the search interval for b'^{ext} is restricted, using typical wall-to-lumen ratio values [2] [7]. Such a simplistic approach can however fail to accurately segment the walls when deformations occur along vessels. Estimating varying half-diameters for inner and outer borders is therefore crucial to take into account these deformations (see Figure 4).

Step 2

We search for the position along the vessels having the largest contrast along the curves defined by the half-diameters b'^{int^*} and b'^{ext^*} found at Step 1. This position is given by

$$i^* = \underset{i}{\operatorname{argmax}} \frac{1}{2} \Big(\bar{D}^{int}(b'^{int^*}, i, r) + \bar{D}^{ext}(b'^{ext^*}, i, r) \Big).$$

Step 3

Finally, we jointly search for a variable half-diameter of inner and outer borders whose difference (the wall thickness) is constant and having the largest contrast along the curves defined by the half-diameters b'^{int^*} and b'^{ext^*} found at Step 1. These half-diameters are constructed iteratively under a regularity constraint from each side of the position i^* found at Step 2. For a fixed gap e, the half-diameter of inner borders b''^{int^*} is constructed as follows:

$$b_i''^{int^*} = \begin{cases} b'^{int^*} & \text{if } i = i^* \\ \operatorname{argmax}_{b_i''^{int}} E(b_i''^{int}, b_{i-1}''^{int^*}, i, e, r) & \text{if } i > i^* \\ \operatorname{argmax}_{b_i''^{int}} E(b_i''^{int}, b_{i+1}''^{int^*}, i, e, r) & \text{if } i < i^*, \end{cases} \quad (8)$$

with

$$E(b_i''^{int}, b_j''^{int^*}, i, e, r) = \alpha \Bigg(\frac{\bar{D}^{int}(b_i''^{int}, i, r)}{\bar{I}^{int}(b_i''^{int}, i, r)} + \bar{D}^{ext}(b_i''^{int} + \bar{e} + e, i, r) \Bigg) + (1 - \alpha)(b_i''^{int} - b_j''^{int^*})^2, \quad (9)$$

where $\bar{e} = (b'^{ext^*} - b'^{int^*})$ and $\alpha \in [0, 1]$ a parameter controlling the amount of regularity. In (9), notice that the term on the left has the same form as (7), except that it concerns a single point. Finally, we search for the best gap with

$$e^* = \underset{e}{\operatorname{argmax}} \sum_{i>0} E(b_i''^{int^*}, b_{i-1}''^{int^*}, i, e, r), \quad (10)$$

and where b''^{int^*} is constructed using (8) and (9). Notice that the discretization step the search intervals of (8) and (10) is divided by two. The half-diameters estimates of inner and outer borders are finally respectively given by $b^{int} = b''^{int^*}$ and $b^{ext} = b''^{int^*} + \bar{e} + e^*$. Rough estimates of inner and outer borders are now fully defined using (3).

B. Refined segmentation

The model proposed in [5] simultaneously evolves two curves under a parallelism constraint. In what follows, we describe an extension of this model for extracting four curves V_1, V_2, V_3 and V_4 almost parallel to a reference line V. Since this line is fixed in our situation, the energy becomes

$$E(V_1, \ldots, V_4, b_1, \ldots, b_4) = \sum_{k=1}^{4} \Big(E_{Image}(V_k) + R(V_k, b_k) \Big), \quad (11)$$

where the term

$$E_{Image}(V_k) = \int_0^1 P(V_k(s))\ ds$$

is designed to attract the curve V_k towards large intensity gradients (see [6]). In this context, the term E_{Image} is based on the Gradient Vector Flow [16]. The role of the term R in (11) is to control the variation of the distance b_k, thus imposing a local parallelism to the reference line V. The authors of [5] proposed a function of the derivative of b_k with

$$R(V_k, b_k) = \int_0^1 Q(s, b_k')\ ds = \int_0^1 \varphi_k(s)(b_k'(s))^2\ ds,$$

where $\varphi_k(s) \in \mathbb{R}^+$ are application-dependent parameters that locally control the strength of the parallelism of the curve V_k with respect to the reference line V. More precisely, the larger the parameter $\varphi_k(s)$ is, the more strict is the parallelism to the reference line V. Notice also that the distance between them has not to be known as prerequisite. It is adjusted during the evolution process and can vary along boundaries. Notice that the energy (11) does not ensure that $b_1(s) < b_3(s)$ and

[2] The wall-to-lumen ratio refers to the ratio between the measurement of the total wall thickness over the measurement of the inner diameter (or lumen).

$b_2(s) < b_4(s)$. However, we never encountered such behavior in our experiments (and for those detailed in Section IV).

Since (11) does not have crossing terms involving different curves, the minimization can be independently done for each curve V_k. For any $k \in \{1, \ldots, 4\}$, the Euler-Lagrange equation expresses the minimization of (11) with respect to $b_k(s)$

$$\frac{\partial P(V_k(s))}{\partial b_k} - \frac{d}{ds}\frac{\partial Q(s, b'_k)}{\partial b'_k} = 0,$$

and the evolution of the distance b_k to the line V is driven by

$$\langle \vec{n}, -\nabla P(V_k(s)) \rangle - 2[\varphi_k(s) b''_k(s) + \varphi'_k(s) b'_k(s)] = 0. \quad (12)$$

The latter equation is solved by discretizing it and introducing the time variable using standard numerical approximations of derivatives (central difference in space, backward difference in time). The resolution of the above equations stops when

$$\max_{k \in \{1,\ldots,4\}} \{\max_s |b_k^n(s) - b_k^{n-1}(s)|\} \leq \varepsilon.$$

In the latter expression, $b_k^n(s)$ is the estimate of the distance of the curve V_k to the reference line V at iteration n and $\varepsilon \simeq 0$ is an accuracy parameter. An example of resolution using this model is illustrated in Figure 4(c).

IV. Evaluation

Thirteen images from healthy subjects were manually delineated by three physicians [3]. These physicians have several years of experience in AO image interpretation. The images were selected to ensure the representativeness of the quality and the noise levels encountered by physicians during routine clinical. Let us respectively denote by V^M and V^A a manual and automatic segmentation. For each image, we measure using the same axial reflection, the absolute relative difference on inner and outer diameters as well as total wall thickness (i.e. the absolute difference between outer and inner diameters), resp. defined for each point by

$$\delta_{int}(V^M, V^A) = \frac{|d_{int}(V^M) - d_{int}(V^A)|}{d_{int}(V^M)} \times 100, \quad (13)$$

$$\delta_{ext}(V^M, V^A) = \frac{|d_{ext}(V^M) - d_{ext}(V^A)|}{d_{ext}(V^M)} \times 100, \quad (14)$$

$$\delta_{wt}(V^M, V^A) = \frac{|d_{wt}(V^M) - d_{wt}(V^A)|}{d_{wt}(V^M)} \times 100, \quad (15)$$

where d_{ext}, d_{int} and d_{wt} denote the outer diameter, the inner diameter and the total wall thickness, respectively. Notice that δ_{wt} is of great importance for us due to its high sensitivity. For consistency, the above measures are only calculated where no bifurcation occurs with other blood vessels (see Figure 5(f)). For the parameters, we set $\varepsilon = 0.1$, $\alpha = 0.9$, $r = 10$ and $\varphi_k = 100$, $\forall k \in \{1, \ldots, 4\}$, for all experiments. Since not enough data were available for measuring the intra-physician variability, we choose the most experienced one as a reference (denoted by Phys_{Ref}). For each image, we then calculated the mean and standard deviation [4] of (13), (14) and (15) along vessels, between manual segmentations as well as between the segmentation obtained by the automatic procedure and the manual segmentations from Phys_{Ref}. The results are detailed in Table I and illustrated in Figure 5. To put in perspective these results, we also provide between parentheses in Table I, these statistics for a displacement of one pixel all along a curve. In that case, the numerator of (13), (14) and (15) becomes equal to one. Due to the size of arterial walls, we first remark that the error is larger for total wall thickness than for inner and outer diameters. Additionally, the error introduced by the automatic procedure is smaller than the inter-physicians error for total wall thickness and inner diameter. Although this error is larger than the inter-physicians error for inner diameter, it remains reasonably near from it. We do believe the poor results obtained for some Subjects (e.g. 3 and 12) are mainly due to a lack of accuracy in the delineation of manual segmentations. Due to the poor contrast along walls and the size of these structures, it is indeed difficult for physicians to precisely delineate them (see Subject 5 in Figure 5(h)). Also, the outer border of walls from the automatic procedure can be sometimes slightly different from manual segmentations. This can be for instance the case when "double contour" occur all along the outer wall border (see Subject 3 in Figure 5(f)). However, there is no clear consensus among physicians about the correct position of the outer wall border in such a situation.

[3] Pathological subjects will be evaluated in a forthcoming paper.

[4] For convenience, we will refer to "error" for both in what follows.

V. Conclusion

In this paper, we have presented a method for segmenting arterial walls in adaptive optics images. Noticeably, the variability introduced by this method is smaller than the inter-physicians variability for wall thickness. We plan to improve the detection of axial reflections and improve the segmentation of walls by introducing extra energy terms in parallel snakes.

References

[1] T.Y. Chan, D.A. Vannasdale, and S.A. Burns. The use of forward scatter to improve retinal vascular imaging with an adaptive optics scanning laser ophthalmoscope. *Bio. Optics Express*, 3(10):2537–2549, 2012.

[2] L.D. Cohen and R. Kimmel. Global minimum for active contour models: A minimal path approach. *International Journal of Computer Vision*, 24(1):57–78, 1997.

[3] A.M. Heagerty et al. Small artery structure in hypertension: dual processes of remodeling and growth. *J. of Hyp.*, 21:391–397, 1993.

[4] N.H. Buus et al. Small artery structure during antihypertensive therapy is an independent predictor of cardiovascular events in essential hypertension. *J. of Hyp.*, 31(4):791–797, 2013.

[5] I. Ghorbel, F. Rossant, I. Bloch, and M. Paques. Modeling a parallelism constraint in active contours. application to the segmentation of eye vessels and retinal layers. In *IEEE International Conference on Image Processing*, pages 445–448, 2011.

[6] M. Kass, A. Witkin, and D. Terzopoulos. Snakes: active contour models. *International Journal of Computer Vision*, 1(4):321–331, 1988.

[7] E. Koch. Morphometric study of human retina arteriolars in high resolution imaging. Master's thesis, Univ. Pierre et Marie Curie, 2012.

[8] E. Koch, D. Rosenbaum, A. Brolly, J.-A. Sahel, P. Chaumet-Riffaud, X. Girard, F. Rossant, and M. Paques. Morphometric analysis of small arteries in the human retina using adaptive optics imaging: relationship with blood pressure and focal vascular changes. *J. of Hyp.*, 2013.

[9] C. Kulcsár, G. Le Besnerais, E. Ödlund, and X. Levecq. Robust processing of images sequences produced by an adaptive optics retinal camera. In *Optical Society of America, Adaptive Optics: Methods, Analysis and Applications*, page OW3A.3, 2013.

[10] J. Liang, D.R. Williams, and D.T. Miller. Supernormal vision and high-resolution retinal imaging through adaptive optics. *Journal of Optical Society America A*, 14(11):2884–2892, 1997.

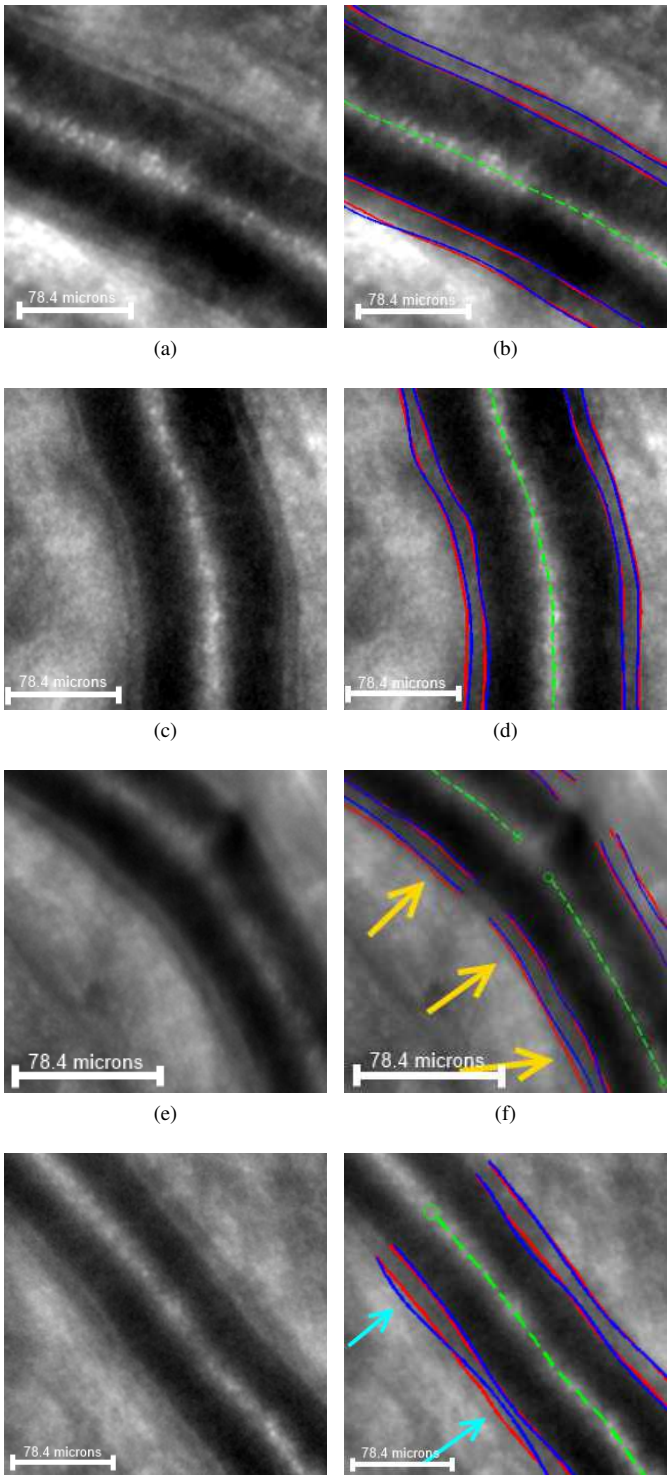

(a) (b) (c) (d) (e) (f) (g) (h)

Figure 5: Positive (a),(b),(c),(d) and negative (e),(f),(g),(h) segmentation results against Phys_{Ref} for Subjects 7 (a),(b), 11 (c),(d), 3 (e),(f) and 5 (g),(h). Automatic segmentations are drawn in red while manual ones are drawn in blue. Green dashed lines correspond to the reference line V. Orange and cyan arrows respectively point misplacement of curves in automatic and manual segmentations.

Subject	Inter-physicians	Our method / Phys_{Ref}
1	2.29 ± 1.54 (1.13 ± 0.04)	2.07 ± 1.06 (1.13 ± 0.04)
2	3.50 ± 2.37 (2.47 ± 0.16)	4.17 ± 3.29 (2.47 ± 0.16)
3	2.86 ± 2.57 (1.37 ± 0.04)	1.63 ± 1.31 (1.37 ± 0.04)
4	2.29 ± 1.7 (0.75 ± 0.03)	3.16 ± 1.65 (0.75 ± 0.03)
5	2.79 ± 1.91 (0.89 ± 0.05)	3.21 ± 2.09 (0.89 ± 0.05)
6	3.75 ± 2.8 (1.13 ± 0.05)	2.14 ± 2.34 (1.13 ± 0.05)
7	2.82 ± 2.38 (0.87 ± 0.04)	2.51 ± 2.64 (0.87 ± 0.04)
8	2.84 ± 2.41 (0.97 ± 0.03)	3.78 ± 2.92 (0.97 ± 0.03)
9	3.26 ± 2.65 (0.87 ± 0.03)	4.58 ± 3.19 (0.87 ± 0.03)
10	3 ± 2.08 (0.8 ± 0.02)	1.87 ± 1.96 (0.8 ± 0.02)
11	2.75 ± 1.8 (0.84 ± 0.02)	2.36 ± 1.88 (0.84 ± 0.02)
12	2.7 ± 2.26 (0.9 ± 0.04)	2.51 ± 2.05 (0.9 ± 0.04)
13	3.38 ± 2.27 (0.84 ± 0.05)	6.07 ± 4.25 (0.84 ± 0.05)
Avg	2.92 ± 2.24 (0.99 ± 0.35)	3.06 ± 2.73 (0.99 ± 0.35)

Subject	Inter-physicians	Our method / Phys_{Ref}
1	2.08 ± 1.69 (0.91 ± 0.02)	2.06 ± 1.83 (0.91 ± 0.02)
2	2.2 ± 1.76 (1.7 ± 0.07)	3.86 ± 1.92 (1.7 ± 0.07)
3	2.16 ± 1.53 (1.05 ± 0.03)	5.64 ± 2.82 (1.05 ± 0.03)
4	2.8 ± 1.94 (0.6 ± 0.02)	1.57 ± 1.04 (0.6 ± 0.02)
5	2.94 ± 2.19 (0.67 ± 0.03)	2.28 ± 1.66 (0.67 ± 0.03)
6	5.11 ± 3.81 (0.74 ± 0.03)	3.05 ± 2.1 (0.74 ± 0.03)
7	4.05 ± 2.59 (0.65 ± 0.01)	1.96 ± 1.38 (0.65 ± 0.01)
8	1.93 ± 1.36 (0.69 ± 0.02)	2.23 ± 1.34 (0.69 ± 0.02)
9	2.93 ± 1.84 (0.62 ± 0.01)	2.33 ± 1.01 (0.62 ± 0.01)
10	3.03 ± 1.97 (0.6 ± 0.01)	1.67 ± 1.45 (0.6 ± 0.01)
11	2.18 ± 1.95 (0.68 ± 0.01)	2.19 ± 1.33 (0.68 ± 0.01)
12	2.48 ± 1.54 (0.69 ± 0.03)	5.04 ± 2.27 (0.69 ± 0.03)
13	1.7 ± 1.28 (0.68 ± 0.02)	2.95 ± 2.68 (0.68 ± 0.02)
Avg	2.83 ± 2.31 (0.74 ± 0.24)	2.7 ± 2.16 (0.74 ± 0.24)

Subject	Inter-physicians	Our method / Phys_{Ref}
1	10.57 ± 8.1 (4.68 ± 0.59)	9.12 ± 6.33 (4.68 ± 0.59)
2	8.78 ± 6.59 (5.53 ± 0.58)	9.79 ± 6.03 (5.53 ± 0.58)
3	11.63 ± 9.54 (4.63 ± 0.45)	23.11 ± 13.1 (4.63 ± 0.45)
4	14.52 ± 11.95 (3.04 ± 0.43)	13.52 ± 8.35 (3.04 ± 0.43)
5	17.46 ± 14.5 (2.8 ± 0.57)	15.62 ± 11 (2.8 ± 0.57)
6	14.32 ± 10.93 (2.2 ± 0.29)	10.9 ± 7.87 (2.2 ± 0.29)
7	16.12 ± 10.57 (2.54 ± 0.33)	9.82 ± 8.59 (2.54 ± 0.33)
8	9.85 ± 7.64 (2.46 ± 0.22)	12.22 ± 6.22 (2.46 ± 0.22)
19	14.77 ± 12.36 (2.17 ± 0.32)	11.42 ± 5.6 (2.17 ± 0.32)
10	13.17 ± 8.52 (2.36 ± 0.23)	7.4 ± 5.87 (2.36 ± 0.23)
11	15.98 ± 13.26 (3.67 ± 0.36)	15.15 ± 13.8 (3.67 ± 0.36)
12	12.58 ± 10.11 (2.88 ± 0.22)	25.52 ± 8.41 (2.88 ± 0.22)
13	15.69 ± 10.53 (3.5 ± 0.4)	14.68 ± 11.8 (3.49 ± 0.4)
Avg	14.09 ± 11.34 (3.1 ± 0.98)	13.84 ± 10.52 (3.1 ± 0.98)

Table I: From top to bottom: inter-physicians and automatic / Phys_{Ref} absolute relative error for inner diameter (see Equation (13)) outer diameter (see Equation (14)) and total wall thickness (see Equation (15)). The numbers between parentheses denote a unit displacement all along the curve.

[11] J.A. Martin and A. Roorda. Direct and noninvasive assessment of parafoveal capillary leukocyte velocity. *Ophthalmology*, 112(12):2219–2224, 2005.

[12] J.A. Sethian. *Level Set Methods and Fast Marching Methods: Evolving Interfaces in Computational Geometry, Fluid Mechanics, Computer Vision, and Materials Science*. Cambridge University Press, 1999.

[13] H. Taylor and J. Keeffe. World blindness: a 21st century perspective. *British Journal of Ophtalmology*, 85(3):261–266, 2001.

[14] C. Viard, K. Nakashima, B. Lamory, X. Paques, M. ad Levecq, and N. Château. Imaging microscopic structures in pathological retinas using a flood-illumination adaptive optics retinal camera. In *Photonics West: Biomedical Optics (BiOS)*, volume 7885, pages 788 509+, 2011.

[15] J. Weickert, B.H. Romeny, and M. Viergever. Efficient and reliable schemes for nonlinear diffusion filtering. *IEEE Transactions on Image Processing*, 7(3):398–410, 1998.

[16] C. Xu and J.L. Prince. Snakes, shapes and gradient vector flow. *IEEE Transactions on Image Processing*, 7(3):359–369, 1998.